Article

Exceptional Mineral Scaling Resistance from the Surface Gas Layer: Impacts of Surface Wetting Properties and the Gas Layer Charging Mechanism

Thomas Horseman and Shihong Lin*

Cite This: *ACS Environ. Au* 2022, 2, 418−427

Read Online

ACCESS | Metrics & More | Article Recommendations | SI Supporting Information

ABSTRACT: Mineral scaling is a phenomenon that occurs on submerged surfaces in contact with saline solutions. In membrane desalination, heat exchangers, and marine structures, mineral scaling reduces process efficiency and eventually leads to process failure. Therefore, achieving long-term scaling resistance is beneficial to enhancing process performance and reducing operating and maintenance costs. While evidence shows that superhydrophobic surfaces may reduce mineral scaling kinetics, prolonged scaling resistance is limited due to the finite stability of the entrained gas layer present in a Cassie−Baxter wetting state. Additionally, superhydrophobic surfaces are not always feasible for all applications, but strategies for long-term scaling resistance with smooth or even hydrophilic surfaces are often overlooked. In this study, we elucidate the role of interfacial nanobubbles on the scaling kinetics of submerged surfaces of varied wetting properties, including those that do not entrain a gas layer. We show that both solution conditions and surface wetting properties that promote interfacial bubble formation enhances scaling resistance. In the absence of interfacial bubbles, scaling kinetics decrease as surface energy decreases, while the presence of bulk nanobubbles enhances the scaling resistance of the surface with any wetting property. The findings in this study allude to scaling mitigation strategies that are enabled by solution and surface properties that promote the formation and stability of interfacial gas layers and provide insights to surface and process design for greater scaling resistance.

KEYWORDS: *nanobubbles, mineral scaling, calcite, wetting, superhydrophobic surface, hydrophilic surface, quartz crystal microbalance*
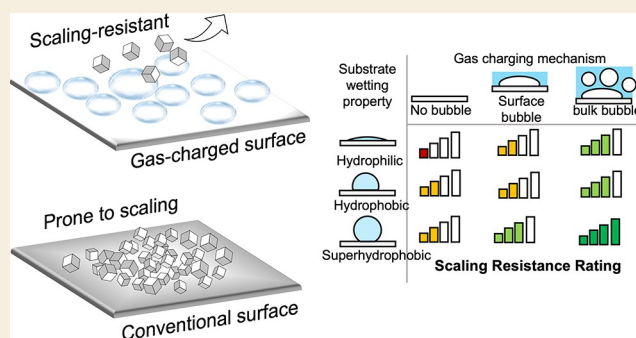
INTRODUCTION

Mineral scaling, or inorganic fouling, is a phenomenon where mineral crystals precipitate out of solution and accumulate on a surface. Mineral crystals can nucleate in the bulk solution and deposit on the surface or nucleate directly on the surface. In either case, the formation and growth of a mineral crystal layer on a surface can be detrimental in different applications, including membrane separations, heat exchangers, and marine structures. For desalination membranes, mineral scaling on membranes reduces water permeability as the crystal layer blocks the membrane pores. In membrane distillation, specifically, mineral scaling can even lead to reduced salt rejection as mineral crystal growth can damage and penetrate the membrane pore structure.[1,2] Mineral scaling on heat exchangers reduces the efficiency of heat exchange between the two process streams as the crystal layer adds heat transfer resistance.[3−6] On marine surfaces such as ship vessels, the formation of a mineral crystal layer adds hydrodynamic resistance, which reduces fuel efficiency.[7−9] In addition to negatively affecting process efficiency, and ultimately increasing operating costs, mineral scaling can also accelerate material corrosion or degradation.[10,11] As scaling can compromise or even cause these processes to fail, the mechanism of mineral scaling and its mitigation strategies have been extensively studied.[12−21]

Common industrially relevant scalants such as gypsum ($CaSO_4−2H_2O$), calcite ($CaCO_3$), and silicates have been extensively studied due to their low solubility and, thus, high propensity to precipitate and form a mineral scaling layer.[2] In the context of membrane distillation, it has been shown that superhydrophobic membranes can significantly reduce mineral scaling by decreasing the propensity for heterogenous crystal nucleation on the surface, reducing the residence time for crystal nucleation, deposition, or growth in the boundary layer near the surface due to the slip boundary condition, and decreasing the solid−liquid contact available for crystal
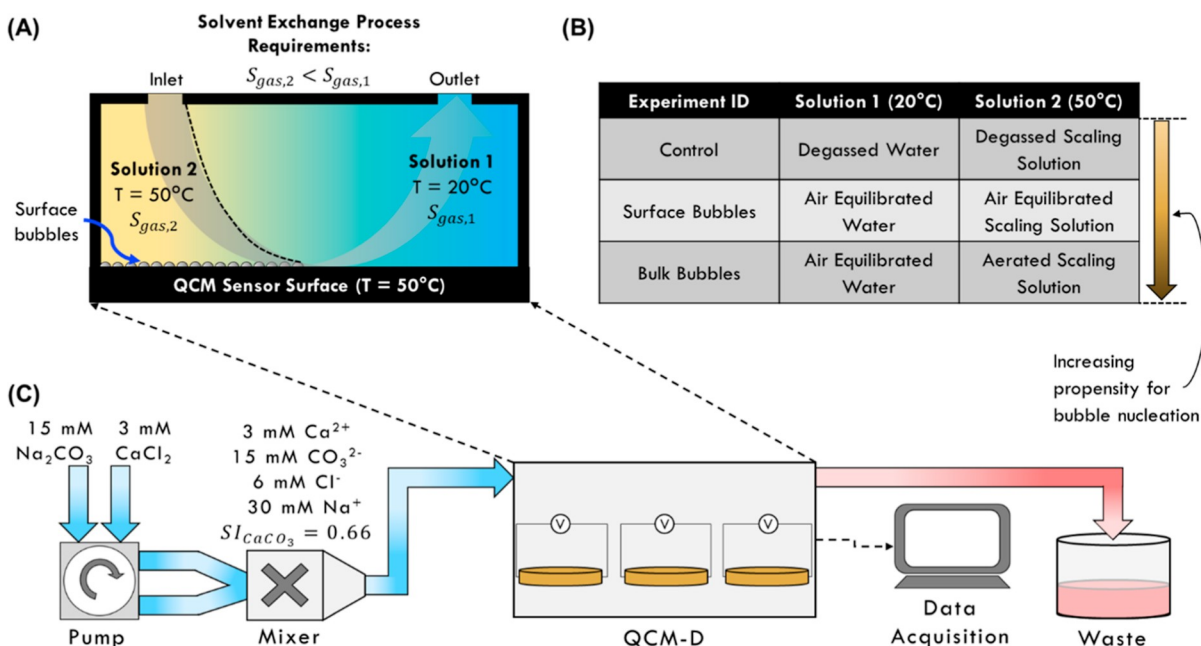
Figure 1. (A) Schematic diagram of the solvent exchange process employed to establish interfacial gas layers in this study. Initially, the QCM cell is heated to 50 °C and the crystal resonances are found in degassed DI water at 50 °C. Then solution 1, at 20 °C with gas solubility, $S_{gas,1}$, is injected into the cell where the sudden change in dissolved gas solubility due to temperature change induces bubble nucleation near the sensor surface. Next solution 2, at 50 °C with gas solubility, $S_{gas,2}$, is injected into the cell. As the gas solubility of solution 2 is less than that of solution 1, that is, $S_{gas,2} < S_{gas,1}$, due to temperature and salinity induced solubility difference, the mixing of the two solutions induces dissolved gas nucleation at the mixing frontier. (B) Description of the solutions used for solvent exchanges. (C) Schematic diagram of the experimental setup used to study the influence of interfacial gas layers on calcium carbonate scaling kinetics with QCM-D.

nucleation and/or deposition and growth on the surface.[2,22,23] More generally, the excellent scaling resistance of superhydrophobic surfaces in the context of membranes,[24−28] heat exchangers,[29−32] and marine surfaces[33] is associated with the Cassie−Baxter wetting state. However, it has also been shown that the Cassie−Baxter states of many systems are metastable, that is, these systems eventually transitioned to the Wenzel state as the entrapped gas layer vanished via gradual gas dissolution or mechanical perturbation.[34−37] Therefore, process optimization to maintain the gas layer and prolong the stability of this Cassie−Baxter wetting state is critical to sustaining long-term scaling resistance.

In addition to superhydrophobic surfaces, which are not necessarily deployable in all contexts, strategies for mitigating mineral scaling on smooth or even hydrophilic surfaces are also of great practical interest. While the intrinsic effects of surface roughness and surface energy on mineral scaling have been elucidated in previous studies,[38−44] the impacts of the presence of surface nanobubbles on scaling resistance have not been fully understood. It has been shown that surface nanobubbles exist on submerged hydrophilic and hydrophobic surfaces and that these bubbles are stable there for days.[45−54] Can we leverage these stable nanobubbles to enhance the scaling resistance of smooth hydrophilic and hydrophobic surfaces that do not intrinsically entrap a gas layer?

In this study, we demonstrate the influence of surface wetting properties and the interfacial gas layer charging on calcium carbonate (CaCO$_3$) scaling kinetics. We employ a well-established solvent exchange process to produce interfacial gas bubbles[46,49,55−58] on quartz crystal microbalance (QCM) sensor surfaces with hydrophilic, hydrophobic, and superhydrophobic wetting properties. We evaluate the degree of interfacial gas layer charging for each surface and compare

the effect of surface wetting property on the effectiveness of interfacial gas layer charging. After generating interfacial gas bubbles using solvent exchange, we expose the gas-charged surfaces to the CaCO$_3$ scaling solution to evaluate how the interfacial gas layer influences the mineral scaling process. We characterize the scaling kinetics in long-term scaling experiments via quartz crystal microbalance with dissipation monitoring (QCM-D) and characterize surface scale morphology with scanning electron microscopy equipped with energy-dispersive X-ray spectroscopy (SEM−EDX). Based on data obtained from the QCM-D experiments and SEM−EDX characterizations, we compare the effectiveness of CaCO$_3$ scaling mitigation between surfaces with different wetting properties and gas-charging mechanisms.

■ MATERIALS AND METHODS

Chemicals

Sulfuric acid (H$_2$SO$_4$, 96% aqueous solution) and hydrochloric acid (HCl, ACS grade, 12M) were purchased from Fisher Scientific (MA, USA) and ethanol (200 proof) was purchased from Decon Labs, Inc. (PA, USA). Acetone (ACS reagent-grade, ≥99.5%), hydrogen peroxide (H$_2$O$_2$, 30 wt %), 1*H*,1*H*,2*H*,2*H*-perfluorodecyltriethoxysilane (FAS, 97%), methyltrichlorosilane (MTS, 99%), and toluene (anhydrous, 99.8%) were all purchased from Millipore Sigma (MA, USA). Calcium chloride (CaCl$_2$, anhydrous, >95%) and sodium carbonate (Na$_2$CO$_3$, anhydrous, ACS Grade) were purchased from Research Products International (IL, USA).

Surface Fabrication and Characterization

All surfaces were created by modifying polished silicon dioxide (SiO$_2$) coated substrates. Specifically, quartz crystal sensors (QSense QSX 303 from Biolin Scientific, SE) were used for QCM-D experiments, and 5 × 5 mm diced SiO$_2$ substrates (Ted Pella, Inc., CA, USA) were used for SEM imaging. To obtain the hydrophilic surface, the SiO$_2$

surface was rinsed with ethanol, acetone, and deionized (DI) Milli-Q water and then placed in a UV/ozone cleaner (M42, Jelight) for 10 min. The plasma cleaned surface was then transferred to a piranha solution (3:1 mixture of H_2SO_4 and H_2O_2) for 20 s. The surface was rinsed with DI water and blown dry with compressed nitrogen gas and immersed in DI Milli-Q water before experiments. This process was repeated every time the hydrophilic surface was used.

To obtain the hydrophobic surface, the SiO_2 surface was first hydroxylated with the hydrophilic treatment stated above. The hydroxylated surface was blown dry with nitrogen gas, heated at 100 °C for 10 min, then immediately placed in a closed Petri dish with multiple drops (10 μL) of 1H,1H,2H,2H-perfluorodecyltriethoxysilane (FAS). The dish was held at 70 °C overnight at negative 0.08 MPa for coating the hydroxylated SiO_2 surface with FAS via chemical vapor deposition.

To obtain the rough and superhydrophobic surface, a three-dimensionally rough hydrophobic film was created by polymerization on the polished SiO_2 surface. First, the SiO_2 surface was hydroxylated with the hydrophilic surface treatment detailed earlier. The surface was blown dry with nitrogen gas and heated at 100 °C for 10 min then immediately placed in toluene with 55 mM methyl trichlorosilane. The reaction vessel was tightly sealed and gently mixed for 3−4 h at room temperature. The surface was then rinsed sequentially with ~25 mL of toluene, ethanol, and DI water; blown dry with compressed nitrogen; and annealed at 100 °C for 5 min.

We compared the wetting properties of the surfaces by measuring the static water contact angle (CA) with an optical tensiometer (T114, Attension). The CA hysteresis was quantified by measuring the sliding angle (SA), that is, the critical tilting angle at which the water droplet de-pins from its original location and slides down the substrate surface.

Solvent Exchange and Scaling Experiments

A well-established solvent exchange method was applied on the three surfaces where a sudden decrease in gas solubility was used to induce bubble nucleation (Figure 1A).[46,49,55−58] First, solution 1, held at 20 °C and with dissolved gas solubility $S_{gas,1}$, was injected at 50 μL min^{-1} into the flow cell that was held at 50 °C. This solution injection is considered the start of the experiment (i.e., $t = 0$). The sudden temperature change in the solution near the surface induces initial gas bubble nucleation due to the gas solubility decrease associated with temperature.[59] After 10 min, solution 2 with bulk gas solubility $S_{gas,2}$, was injected also at 50 μL min^{-1} into the flow cell at 50 °C. Solution 2 has a lower gas solubility than solution 1 ($S_{gas,1}/S_{gas,2} \sim 10^1$ to 10^3) due to the reduction in solubility by temperature and salinity, so the sudden change in gas solubility at the mixing frontier resulted in more nanobubble nucleation on or near the sensor surface.[56] More detailed explanations of the mechanism of bubble nucleation by this solvent-exchange method can be found in recent studies using this method.[46,49,55−58]

In the control experiment, both solution 1 and solution 2 were degassed overnight under vacuum at −0.08 MPa gauge pressure and elevated temperature (50 °C, Figure 1B). As such, no dissolved gas was present to nucleate on the surfaces, and thus, any frequency or dissipation response during the solvent exchange was caused by changes in bulk solution properties (discussed in more detail later). These values were subtracted from the surface bubble and bulk bubble experiments to isolate the response due to nanobubble nucleation and/or adsorption. In the reference experiment, solution 1 was ethanol while solution 2 was water. The ethanol/water solvent exchange has been utilized extensively in the literature to induce nanobubble nucleation including fundamental studies using QCM-D.[55,60] The reference experiment served to validate the protocol and observations in this study.

The control, surface bubbles, and bulk bubbles experiments were strategically selected with an increasing propensity for bubble nucleation and adsorption, and thus surface bubble coverage (Figure 1B). For example, both solutions 1 and 2 in the control experiment were degassed, and thus no dissolved gases were present for bubble nucleation, while in the surface and bulk bubble experiments, the gas

solubility ratio between solutions 1 and 2 was on the order of 10^3.[61−63] Furthermore, solution 2 in the bulk bubble experiment was aerated with nitrogen gas with a nanobubble generator (25 nanoBoost with NPE pump, Moleaer Inc., NY, USA), giving the highest propensity for bubble coverage as bulk bubbles may also adsorb to the surface from the bulk.[54,64,65] The aerated solutions contained $1 \pm 0.2 \times 10^8$ mL^{-1} of nanobubbles averaging 183 ± 11 nm in diameter (Figure S1, Malvern Nanosight NS300, UK).

In the control, surface bubble, and bulk bubble experiments, the solvent exchanges were first conducted with the respective solutions listed in Figure 1B to establish gas bubbles (or the lack thereof in the case of the control) on the surfaces. Immediately following the solvent exchanges, and without removing the solution from the cell, solution 2 continued to flow over the sensor surface for a total of 7 h to elucidate the effect of surface bubble coverage on mineral scaling. The scaling solutions were prepared by mixing a solution of 3 mM calcium chloride ($CaCl_2$) and a solution of 15 mM sodium carbonate (Na_2CO_3). Prior to mixing, the water was degassed (control), air equilibrated (surface bubbles), or aerated (bulk bubbles), held at 50 °C, and sealed from the ambient environment. The solutions were pumped to a mixer just before the QCM-D cell to form a saturated calcium carbonate scaling solution that then flowed into separate QCM-D cells over the fabricated sensor surfaces (Figure 1C). The saturation index (SI) was calculated as 0.66 by PHREEQC (v3.4, USGS, as the log10 of ion activity product divided by the solubility product), which is converted to an SI of ~1.52 if the natural log convention is used.

Quartz Crystal Microbalance Experiments

The solvent exchange and scaling experiments were conducted using a quartz crystal microbalance with dissipation monitoring (QSense E4 Analyzer, Sweden). After surface modification, the quartz crystal sensors were transferred to their respective flow cells, which were held at 50 °C. Degassed deionized MilliQ water, held at 50 °C, was then injected into the cell at 50 μL min^{-1} for 10 min to equilibrate the sensor. After equilibration, the sensor's resonant frequencies were found using the QSense Dfind software, and a stable baseline was established (≤2 Hz frequency drift and ≤0.2 × 10^{-6} dissipation drift). Sensors that deviate from a stable baseline were replaced. After establishing stable baselines, the frequency and dissipation responses were recorded over the entire solvent exchange and scaling experiments and analyzed with the QSense Dfind software.

Mineral Scaling Characterization

Polished SiO_2 wafers (5 × 5 mm diced SiO_2 substrates from Ted Pella, Inc., CA, USA) were subject to identical surface fabrication procedures mentioned previously to produce hydrophilic, hydrophobic, and superhydrophobic wetting properties. These wafers were then inserted into a closed flow cell and subjected to identical solvent exchange and scaling experimental conditions. To analyze the morphology of the mineral crystal layer after scaling experiments, the scaled surfaces were immediately removed from the flow cell and excess solution was blown off the surfaces with compressed nitrogen. The surfaces were imaged via a scanning electron microscope fitted with an energy dispersive X-ray detector (Merlin, Zeiss, DE).

■ RESULTS AND DISCUSSION

QCM-D Response to Gas Layer Formation and Mineral Scaling

In all experiments, QCM with dissipation monitoring was used to evaluate the effect of surface wetting properties and solution conditions on gas bubble surface coverage during the solvent exchanges. After the solvent exchanges, the scaling solution continued to flow over the quartz crystal sensors and QCM-D was used to elucidate the effect of gas bubble surface coverage on mineral scaling. For rigid mass coupling with the sensor surface, should it be liquid, gas bubbles, or mineral crystals, mass adsorption follows the Sauerbrey relationship (eq 1).[66]
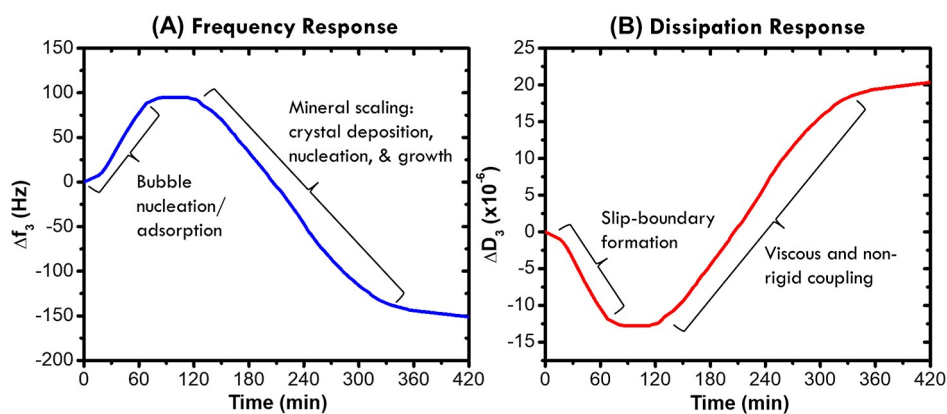
Figure 2. Representative QCM-D data including (A) frequency and (B) dissipation responses in QCM-D scaling experiments. Initially, the solvent exchanges from Figure 1B were conducted in the first 10 min of the experiment, inducing positive frequency shifts as gas nanobubbles deplete water from the sensor surface. The positive frequency shift is indicative of the water layer at the sensor surface being replaced by the less dense gas bubbles. As bubbles nucleate and adsorb to the sensor surface, dissipation response decreases due to a slip-boundary formation that alleviates viscous energy dissipation that occurs when the sensor is in contact with purely liquid. Eventually, the surface bubble layer equilibrates, and the frequency and dissipation responses stabilize for a short period of time (30−60 min) until mineral crystal nucleation/deposition occurs, resulting in a negative frequency shift and positive dissipation shift. The negative frequency shift is caused by the denser mineral crystals replacing liquid or gas at the sensor surface, while the positive dissipation shift is due to nonrigid coupling between mineral crystals and the QCM sensor surface.

$$\Delta f_n = -\frac{n}{C}\Delta m \tag{1}$$

where Δf_n is the change in the resonant frequency of the quartz crystal oscillator upon adsorption of mass (in Hz), n is the overtone order relative to the first harmonic resonant frequency (dimensionless), C is the mass sensitivity constant (-17.7 ng Hz^{-1} cm^{-2} for the 5 MHz crystals used in this work), and Δm is the areal mass density (in ng cm^{-2}).[67] We note that the rigid film approximation, empirically limited to $\Delta D_n/\Delta f_n < 10^{-7}$ Hz^{-1} by the manufacturer, where ΔD_n is the change in energy dissipation (dimensionless), is satisfied for all experiments. Thus, the rigid film assumption that validates the Sauerbrey relationship holds for all surface mass adsorption/desorption in this study.[67,68] In general, surface bubble nucleation and adsorption cause a positive frequency shift as denser liquid mass is replaced by gaseous mass at the sensor surface, while mineral scaling results in a negative frequency shift as liquid/gaseous mass are replaced by the denser mineral crystals at the sensor surface (Figure 2A). This is a commonly observed phenomenon that can be well explained by the Sauerbrey equation (eq 1).[55,60,69,70]

Along with validating the rigid film approximation, dissipation monitoring provides insight into the rigidity of the coupling between absorbed mass and the sensor surface.[67] In general, mineral crystal nucleation and/or deposition on the sensor surface increased dissipation, indicating an increasing nonrigid coupling between the mineral crystals and sensor surface (Figure 2B). Interestingly, surface bubble nucleation and adsorption resulted in a negative dissipation shift, indicating a "more rigid" coupling between the bubble-covered surface and liquid. This phenomenon is most likely caused by the significant reduction in frictional drag between the liquid and sensor surface as nanobubbles displace water at the interface.[55] For a bubble-free liquid−solid surface coupling with the hydrophilic and hydrophobic surfaces in this study, the nonslip boundary condition tethers liquid to the sensor surface and results in positive dissipation due to energy dissipation via viscous force. However, the presence of surface gas bubbles reduces such tethering and may even create a slip-

boundary condition at the liquid−sensor interface that minimizes viscous energy dissipation.

In liquids, the frequency response is proportional to the square root of bulk liquid viscosity and density (eq 2).[71−73]

$$\Delta f_n = -\frac{1}{C}\sqrt{\frac{n\rho_l\eta_l}{2\omega_F}} \tag{2}$$

where ρ_l is the bulk liquid density, η_l is the bulk liquid viscosity, and ω_F is the angular fundamental resonance frequency. According to eq 2, the changes in liquid density and viscosity (which are both temperature and salinity dependent) from solutions 1 and 2 should induce a change in resonant frequency. In the control experiment, the solutions were degassed, that is, dissolved gases present for possible bubble nucleation or adsorption were removed, to quantify the effect of changing solution density and viscosity on frequency response according to eq 2. Any frequency or dissipation shift measured during the control experiment was subtracted from the frequency or dissipation shifts measured during the surface bubble and bulk bubble solvent exchanges to isolate the nanobubble specific responses, that is, the impacts of liquid density and viscosity variations (as described by eq 2) have been accounted for so that the reported positive frequency shifts are only results of adsorption of gas bubbles (as describe by eq 1).

Surface Wetting Properties

Hydrophilicity was imparted on a polished silicon dioxide quartz crystal surface by hydroxylating with UV/Ozone plasma and a short piranha etch. Complete wetting of the hydrophilic surface was indicated by a contact angle (CA) of zero (Figure 3A). Another polished silicon dioxide quartz crystal was hydroxylated, and long-chain fluoroalkyl-silane (FAS) was grafted to it via chemical vapor deposition to produce a hydrophobic surface. The measured sessile drop CA of 107 ± 3° indicates hydrophobicity (Figure 3B). For either surface, the sliding angle (SA) was too high to be measured, meaning the droplet stayed pinned to the surface even when it was completely inverted. This indicates the presence of strong interaction between water and the sensor surface which leads
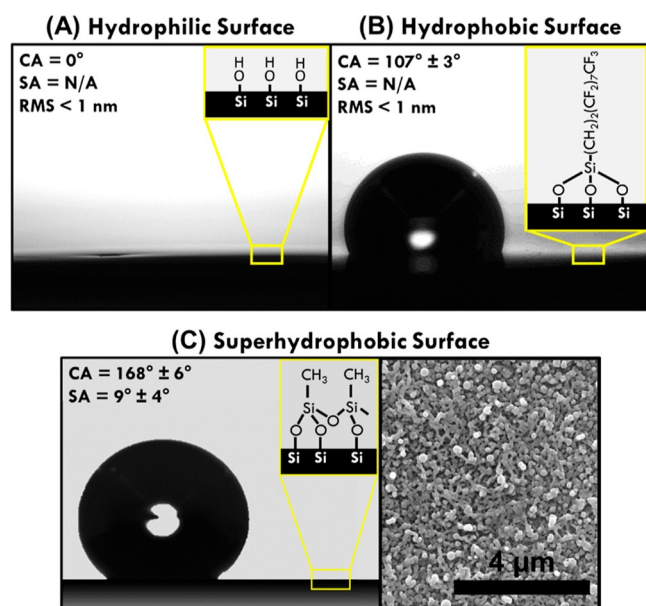
Figure 3. Wetting properties of the smooth (A) hydrophilic and (B) hydrophobic surfaces and the rough (C) superhydrophobic surface. Contact angle (CA), sliding angle (SA), or the minimum tilt angle required to cause a droplet to unpin from the surface, and surface roughness reported as the root mean square (RMS) surface roughness in the top left of panels (A) and (B). The SA was unmeasurable on both hydrophilic and hydrophobic surfaces as the water stayed attached to the surface even when inverted. SEM image of the rough superhydrophobic surface in (C) shows the rough nanoporous 3D methyl siloxane polymer network. Insets show the surface chemistry employed to achieve the desired wetting properties.

to a nonslip boundary condition for water flow along the surface. We note that the hydrophilic and hydrophobic quartz crystal surfaces were both polished to a root-mean-square (RMS) surface roughness of less than 1 nm and that the hydrophilic and hydrophobic surface treatments did not increase the surface roughness of the sensors.[74,75]

Superhydrophobicity was imparted on a polished silicon dioxide quartz crystal by immersing the hydroxylated surface in toluene containing methyl trichlorosilane. A contact angle (CA) of $168 \pm 6°$ and a sliding angle (SA) of $9 \pm 4°$ were measured (Figure 3C left), indicating the achievement of superhydrophobicity (typically defined by a sessile drop CA > 150° and an SA < 10°). The three-dimensional polymer network that forms upon methyl trichlorosilane reaction with the hydroxylated surface creates a rough, nano-porous structure with multiscale roughness that entrains a metastable gas layer upon which the contacting liquid is suspended (Figure 3C right).[76] In such a Cassie−Baxter wetting state, the small fraction of contact between the solid surface and the liquid (f) can be estimated using the Cassie−Baxter equation (eq 3).[77,78]

$$\cos \theta_A = f(\cos \theta_0 + 1) - 1 \qquad (3)$$

where θ_A is the apparent CA and θ_0 is the intrinsic CA (i.e., the CA on a molecularly smooth surface made of the same material as the rough surface that yields θ_A). While we do not know the exact θ_0 for a smooth methyl trichlorosilane-treated surface, it should be lower than that of the FAS-grafted smooth surface (i.e., 107°) because a long-chain fluoroalkyl group is more hydrophobic than a methyl group due to both chain length and moiety. However, even if we assume the methyl trichlorosilane-

treated surface also has θ_0 of 107° (should be lower in reality), applying eq 3 with a measured θ_A of 168° results in an aerial fraction of a solid-water contact (f) of 3%. With a lower θ_0 for methyl trichlorosilane-treated surface, f is likely even smaller. Thus, the interfacial contact on the superhydrophobic surface is dominated by the entrapped gas layer, which possesses at least 97% of the interfacial contact with the liquid.

Gas Layer Formation: Impacts of Surface Wetting Property and the Bubble Generation Method

The solvent exchange solutions were chosen to systematically study the effect of surface wetting properties on gas layer surface coverage. QCM-D was used to semi-quantitatively monitor the extent of surface bubble coverage; as the less dense bubbles replaced a volume of water at the sensor surface, the frequency of the oscillating system increased (eq 1). The magnitude of the positive frequency shifts increased as the propensity for surface bubble coverage increased, as expected by the experimental design (Figure 4). For example, in the
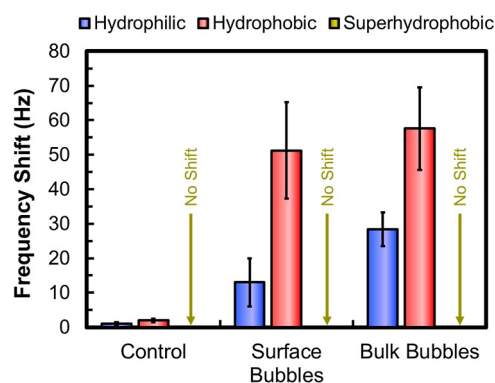
Figure 4. Positive frequency shifts observed on hydrophilic (blue), hydrophobic (red), and superhydrophobic (dark yellow) surfaces, as shown in Figure 3, after the control, surface bubbles, and bulk bubble experiment solvent exchanges from Figure 1B. The positive frequency shifts observed in the control experiments were subtracted from the surface bubble and bulk bubble frequency shifts to remove any response measured due to the changing solution densities and viscosities during the solvent exchanges. The maximum positive frequency shift was recorded after the surface bubble layer equilibrated and frequency response remained constant for at least 30 min. No positive frequency shifts were observed on the superhydrophobic surface. Error bars reflect the standard deviation over three trials.

control experiment, where the solutions were degassed and has no propensity for bubble nucleation, there was little to no positive frequency shift observed, while in the surface bubble and bulk bubble experiments, where the ratio of dissolved gas solubility was on the order of 10^3, noticeable positive frequency shifts were observed.

The magnitude of the positive frequency shift increased from 13 ± 7 Hz on the hydrophilic surface in the surface bubble experiment to 28 ± 5 Hz in the bulk bubble experiment likely because of increased surface bubble coverage as bubbles adsorbed from the bulk solution.[60] While the magnitude of the average positive frequency shift on the hydrophobic surface did slightly increase from 51 ± 14 Hz in the surface bubble experiment to 58 ± 12 Hz in the bulk bubble experiment, these values are relatively similar within experimental error. This is likely because the hydrophobic surface was nearly saturated with adsorbed bubbles in both the surface and bulk bubble
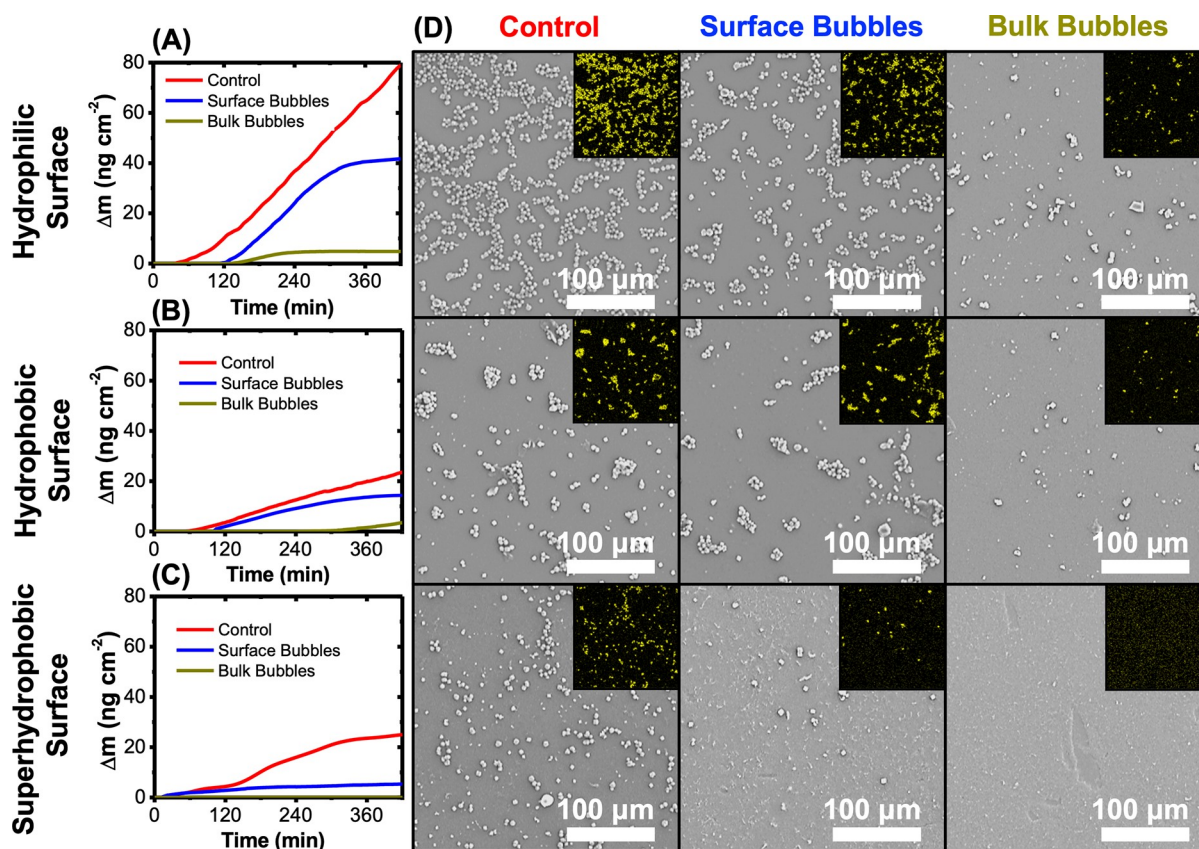
Figure 5. Areal mass density of scale accumulated on (A) hydrophilic, (B) hydrophobic, and (C) superhydrophobic surfaces in long-term scaling experiments measured via QCM-D. (D) SEM images of the scaled surfaces after the scaling experiments in (A−C). The inset shows an EDX map of calcium (yellow) on the surface. The experiment IDs refer to the initial solvent exchanges according to Figure 1B. Degassed deionized (DI) water was used to find the crystal resonances and establish a stable baseline for ∼10 min, then the solvent exchange was conducted to produce an interfacial gas layer. The scaling solution flowed at 50 μL min^{-1} over the sensors for a total of 7 h after said solvent exchange. The baseline for mass accumulation began once the surface bubble layer equilibrated and the frequency response stabilized for at least 30 min (Figure S3).

experiments. We note that the positive frequency shifts measured on the hydrophobic surfaces were consistently larger than those measured on the hydrophilic surfaces (Figure 4), which is consistent with previous studies.[55] This phenomenon can be explained by a combination of two effects (1) propensity for bubble nucleation on the hydrophobic surface was greater due to the lower energy barrier for nucleation.[79] and (2) long-range hydrophobic−hydrophobic interaction between the gas bubbles and hydrophobic surface favors bubble adsorption from the bulk.[80] While the effects of the solvent exchanges were readily observed on the smooth hydrophilic and hydrophobic surfaces, they did not produce positive frequency shifts on the superhydrophobic surface (Figure 4). This is likely because a gas layer is intrinsically present in a submerged superhydrophobic surface and any bubbles that nucleated or adsorbed on the superhydrophobic surface rapidly coalesced into the entrapped gas layer already present there.

In the reference experiment, where the ratio of dissolved gas solubility between solution 1 (ethanol) and solution 2 (water) was on the order of ∼10^1, a positive frequency shift of 4 ± 1 Hz on the hydrophilic surface and 38 ± 8 Hz on the hydrophobic surface were observed (Figure S2). The magnitudes of the shifts in the reference experiment were very similar to what has been reported for similar surfaces, identical solvent exchanges, and with the same QCM-D instrument.[55] Notably, the positive frequency shifts in the

reference experiment were also less than what was observed in the surface bubbles and bulk bubbles experiments, where the ratio of dissolved gas solubility between solution 1 (water) and solution 2 (scaling solution) was on the order of ∼10^3. This evidence not only serves to validate our experimental observations but gives support that increasing dissolved gas solubility difference between solution 1 and solution 2 produces a higher positive frequency shift and, thus, results in more interfacial gas bubble formation.

Impacts of Gas Layer Formation on Mineral Scaling Kinetics

After solvent exchange, the mineral scaling solution (i.e., solution 2 in the control, surface bubbles, and bulk bubbles experiments) flowed over the sensor surface for a total of 7 h to allow the study of the effect of the surface bubble coverage on the mineral scaling process. As surface bubbles or water are replaced by the denser mineral crystals at the sensor surface, a negative frequency shift was observed (Figure S3 top row). While mineral crystal mass deposition did tend to form a less rigid film, as indicated by the positive dissipation shifts (Figure S3 bottom row), the rigid film approximation held in all experiments and, thus, the Sauerbrey equation was used to model the mass accumulation on each surface (eq 1). We note that the reference solvent exchange was carried out for a total of 8 h and showed that the submerged gas layer was stable for the entire experiment (Figure S4). This long-term gas bubble

stability on submerged surfaces has also been well documented in the literature.[45,53,81]

In these experiments, the control represents the scaling response in the absence of a surface bubble layer, while the surface bubble coverage increased from the surface bubble experiment to the bulk bubble experiment for both the hydrophilic and hydrophobic surfaces (Figure 5). As surface bubble coverage increased, mineral scaling kinetics decreased. Specifically, the induction time for mineral nucleation/ deposition, indicated by the onset of mass accumulation on the surface, became longer as the surface bubble coverage increased (Figure 5A,B). Likewise, the final mass of crystals deposited on the surface decreased with the surface bubble coverage. The trend between crystallization kinetics and surface bubble coverage holds true for different solvent exchanges on the same surface or for the same solvent exchange on different surfaces. We believe the mass growth results from the growth of calcite crystals on the surface (which may involve the deposition of nucleates with negligible mass) rather than the deposition of calcite particles formed in the bulk via homogeneous nucleation. This speculation is based on the observation of significant induction time in most experiments (Figure 5A−C). If deposition of particles was the major mechanism, mass growth should be detected at the start of the experiment considering that the solution only passes through the test cell once and that the hydraulic retention time is estimated to be only 2.2 min. Our experiments were designed to intentionally minimize the time for crystal formation by mixing the solutions right before they enter the QCM cell chamber. Regardless of the scaling mechanism, the comparison of scaling kinetics of surfaces with different wetting properties and gas-charging mechanisms is of practical significance.

For the superhydrophobic surface, a positive frequency shift was not observed upon the introduction of the solvent or bubbles, likely because the submerged superhydrophobic membrane spontaneously bore an air film that led to the slip boundary condition even without bubble introduction. However, even with a superhydrophobic surface, the introduction of surface or bulk bubbles still contributes to enhanced scaling resistance (Figure 5C). Likewise, in experiments with other surfaces, mitigation of scaling on a superhydrophobic membrane was more effective with bulk bubbles than with surface bubbles. Interestingly, the final mineral crystal mass deposited on a superhydrophobic surface after the control solvent exchange (i.e., with degassed solutions) was very similar to that on the hydrophobic surface. With a degassed solution flowing over the superhydrophobic surface, there was a large driving force for the entrapped gas layer to destabilize and dissolve into the degassed solution and promote a transition from the Cassie−Baxter to the Wenzel wetting state. At the Wenzel state, scaling kinetics was even slightly faster on the "superhydrophobic" surface compared to the smooth hydrophobic surface, likely because (1) the surface energy of short-chain methyl-terminated surfaces is higher than long-chain perfluorinated surfaces; and (2) the wetted superhydrophobic surface, due to its porosity, has a higher specific surface area than the smooth hydrophobic surface.

Images of the final mineral scaling layer on each surface obtained via the SEM−EDX reveals the mineral crystal surface coverage decreased as the surface bubble coverage increased, supporting the findings from QCM-D experiments (Figure 5D). Furthermore, there was a strong correlation between final

mineral crystal mass measured via QCM-D and mineral crystal areal surface coverage measured from SEM−EDX images (Figure 6). For example, the final mass measured via QCM-D
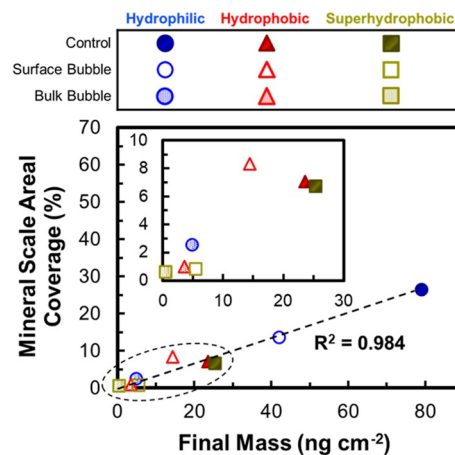
Figure 6. Percentage of the total area covered by mineral crystals measured from SEM−EDX images in Figure 5D using particle size analysis in ImageJ software versus the final crystal mass deposited on the surface according to measured frequency response with QCM-D in Figure 5A−C. The inset shows the highlighted region in the low final mass/areal coverage range. The legend mentioned above matches each symbol with their experimental ID and surface wetting properties. The correlation (R^2) calculated between mineral scale areal coverage measured from SEM−EDX images and final mass measured from QCM-D data for all experiments is displayed with a linear trendline.

on the hydrophilic surface with the control solvent exchange (80 ng cm^{-2}) was approximately twice that measured on the hydrophilic surface with the surface bubble solvent exchange (41 ng cm^{-2}, Figures 5A and 6). SEM−EDX mapping confirms that approximately half the amount of mineral crystal was deposited on the hydrophilic surface during the surface bubble solvent exchange compared to the control solvent exchange with degassed solution (Figure 6). A similar correlation was observed between the hydrophilic (Figure 5A) and hydrophobic (Figure 5B) surfaces with the same solvent exchange. For example, approximately half the mineral crystal deposition was observed on the hydrophobic surface as compared to the hydrophilic surface in the absence of a submerged gas layer in the control solvent exchange experiment (Figures 5D and 6).

The final mineral crystal mass deposited on the superhydrophobic surface after the surface bubble experiment (5 ng cm^{-2}, Figure 5C) was much less than that on the hydrophobic surface (14 ng cm^{-2}, Figure 5B). This is likely caused by the larger degree of gas−liquid contact at the superhydrophobic surface induced by the Cassie−Baxter wetting state as compared to the Wenzel wetting state on the hydrophobic surface with discrete nanobubble coverage. More importantly, virtually no mineral crystal mass accumulation on the superhydrophobic surface was detected by QCM-D or SEM−EDX after the bulk bubble solvent exchange (Figure 5C,D). The adsorption and coalescence of bulk nanobubbles continuously recharged the entrapped gas layer on the superhydrophobic surface, thereby maintaining a robust Cassie−Baxter state and contributing to exceptional long-term scaling resistance.

The observed trend of improved mineral scaling resistance by increasing the surface hydrophobicity of the smooth

surfaces can be explained by a reduced propensity for crystal nucleation and growth on the more hydrophobic surface.[2] This is true in the absence of a surface bubble layer in the control experiments where the intrinsic surface energy of the hydrophobic surface alone reduced the propensity for mineral crystal nucleation relative to that of the hydrophilic surface. However, in the presence of interfacial bubbles in both the surface bubble and bulk bubble experiments, mineral scaling kinetics were even slower on the hydrophobic surface than in the control experiment or the same solvent exchanges on the hydrophilic surfaces. The exceptional scaling resistance was attributable to the enhanced degree of interfacial bubble formation on the hydrophobic surface. Surface bubbles physically shielded the surface from mineral crystal nucleation or deposition as they reduced the area of solid−liquid contact.

CONCLUSIONS AND IMPLICATIONS

From this study, we can draw four main conclusions. (1) Regardless of surface wetting properties, the scaling resistance induced by the solvent exchanges followed the order bulk bubble > surface bubble > no bubble (control). A higher degree of interfacial bubble formation reduces the direct liquid−solid contact for mineral crystal deposition; (2) when solution conditions are conducive to surface or bulk bubble formation, that is, not degassed, the scaling resistance of the surfaces follows the order superhydrophobic > hydrophobic > hydrophilic. This is because increasing hydrophobicity promotes interfacial gas layer stability on submerged surfaces; (3) in the absence of interfacial gas layers, scaling resistance decreases with increasing surface energy; and (4) incorporation of bulk nanobubbles into a scale-prone solution can improve the scaling resistance of any surface regardless of wetting properties. Furthermore, the incorporation of bulk nanobubbles into a scale-prone solution in contact with a superhydrophobic surface virtually eliminates mineral scaling as bulk bubbles coalesce into the entrained gas layer of the superhydrophobic surface and maintain its long-term stability. Bulk nanobubbles may also stabilize a suspension of bulk precipitated mineral crystals via a flotation effect, leading to further enhancement in scaling resistance regardless of surface properties.[82,83]

Implications from these findings may help optimize the combination of surface wetting properties and operating conditions for membrane processes, heat exchangers, and marine structures that are prone to mineral scaling. For example, intermittent solvent exchanges or other operational techniques that promote surface nanobubble nucleation, such as surface localized temperature changes, may prolong the scaling resistance of the surface. While the best scaling resistance can be realized with a superhydrophobic surface, the stability of the Cassie−Baxter state directly relates to the lifetime of the surface's scaling mitigation capabilities. As such, the use of degassed solutions, where the driving force for the entrapped gas layer to dissolve into solution is high, should be avoided. In the best case, regardless of the surface wetting property requirements, mineral scaling can be avoided by aerating with an inert gas such as nitrogen.[84] The presence of bulk bubbles not only prolongs and enhances the surface coverage of adsorbed and nucleated surface bubbles but also exhibits antifouling effects in the bulk via a floatation mechanism.

ASSOCIATED CONTENT

Supporting Information

The Supporting Information is available free of charge at https://pubs.acs.org/doi/10.1021/acsenvironau.2c00011.

Details on bulk nanobubble size distribution, positive frequency shifts relative to a reference study at similar conditions, frequency and dissipation shifts for the solvent exchange and scaling experiments, and a control solvent exchange highlighting the stability of the surface nanobubble layer generated via solvent exchange (PDF)

AUTHOR INFORMATION

Corresponding Author

Shihong Lin − *Department of Chemical and Biomolecular Engineering, Vanderbilt University, Nashville, Tennessee 37235, United States; Department of Civil and Environmental Engineering, Vanderbilt University, Nashville, Tennessee 37235, United States;* orcid.org/0000-0001-9832-9127; Phone: +1 (615) 322-7226; Email: shihong.lin@vanderbilt.edu

Author

Thomas Horseman − *Department of Chemical and Biomolecular Engineering, Vanderbilt University, Nashville, Tennessee 37235, United States;* orcid.org/0000-0002-4660-1448

Complete contact information is available at:
https://pubs.acs.org/10.1021/acsenvironau.2c00011

Notes

The authors declare no competing financial interest.
DISCLAIMER: The views expressed herein do not necessarily represent the views of the U.S. Department of Energy or the United States Government.

REFERENCES

(1) Christie, K. S. S.; Yin, Y.; Lin, S.; Tong, T. Distinct Behaviors between Gypsum and Silica Scaling in Membrane Distillation. *Environ. Sci. Technol.* **2020**, *54*, 568−576.

(2) Horseman, T.; Yin, Y.; Christie, K. S.; Wang, Z.; Tong, T.; Lin, S. Wetting, Scaling, and Fouling in Membrane Distillation: State-of-the-Art Insights on Fundamental Mechanisms and Mitigation Strategies. *ACS ES&T Engg.* **2021**, *1*, 117−140.

(3) Herz, A.; Malayeri, M. R.; Müller-Steinhagen, H. Fouling of Roughened Stainless Steel Surfaces during Convective Heat Transfer to Aqueous Solutions. *Energy Convers. Manag.* **2008**, *49*, 3381−3386.

(4) Al-Janabi, A.; Malayeri, M. R. Innovative Non-Metal Heat Transfer Surfaces to Mitigate Crystallization Fouling. *Int. J. Therm. Sci.* **2019**, *138*, 384−392.

(5) Watkinson, A. P.; Martinez, O. Scaling of Heat Exchanger Tubes by Calcium Carbonate. *J. Heat Transfer* **1975**, *97*, 504−508.

(6) Oon, C. S.; Kazi, S. N.; Hakimin, M. A.; Abdelrazek, A. H.; Mallah, A. R.; Low, F. W.; Tiong, S. K.; Badruddin, I. A.; Kamanger, S. Heat Transfer and Fouling Deposition Investigation on the Titanium

Coated Heat Exchanger Surface. *Powder Technol.* **2020**, *373*, 671−680.

(7) Gittens, J. E.; Smith, T. J.; Suleiman, R.; Akid, R. Current and Emerging Environmentally-Friendly Systems for Fouling Control in the Marine Environment. *Biotechnol. Adv.* **2013**, *31*, 1738−1753.

(8) Deng, R.; Shen, T.; Chen, H.; Lu, J.; Yang, H.-C.; Li, W. Slippery Liquid-Infused Porous Surfaces (SLIPSs): A Perfect Solution to Both Marine Fouling and Corrosion? *J. Mater. Chem. A* **2020**, *8*, 7536−7547.

(9) Genzer, J.; Efimenko, K. Recent Developments in Superhydrophobic Surfaces and Their Relevance to Marine Fouling: A Review. *Biofouling* **2006**, *22*, 339−360.

(10) Yang, D.; Liu, J.; E, X.; Jiang, L. Experimental Study of Composition and Influence Factors on Fouling of Stainless Steel and Copper in Seawater. *Ann. Nucl. Energy* **2016**, *94*, 767−772.

(11) *Corrosion and Fouling Control in Desalination Industry*; Saji, V. S., Meroufel, A. A., Sorour, A. A., Eds.; Springer Nature: Switzerland, 2020.

(12) Christie, K. S. S.; Horseman, T.; Lin, S. Energy Efficiency of Membrane Distillation: Simplified Analysis, Heat Recovery, and the Use of Waste-Heat. *Environ. Int.* **2020**, *138*, 105588.

(13) Christie, K. S. S.; Horseman, T.; Wang, R.; Su, C.; Tong, T.; Lin, S. Gypsum Scaling in Membrane Distillation: Impacts of Temperature and Vapor Flux. *Desalination* **2022**, *525*, 115499.

(14) Andritsos, N.; Karabelas, A. J. Calcium Carbonate Scaling in a Plate Heat Exchanger in the Presence of Particles. *Int. J. Heat Mass Tran.* **2003**, *46*, 4613−4627.

(15) Amjad, Z. Calcium Sulfate Dihydrate (Gypsum) Scale Formation on Heat Exchanger Surfaces: The Influence of Scale Inhibitors. *J. Colloid Interface Sci.* **1988**, *123*, 523−536.

(16) Gill, J. S.; Nancollas, G. H. Kinetics of Growth of Calcium Sulfate Crystals at Heated Metal Surfaces. *J. Cryst. Growth* **1980**, *48*, 34−40.

(17) Hasson, D.; Zahavi, J. Mechanism of Calcium Sulfate Scale Deposition on Heat Transfer Surfaces. *Ind. Eng. Chem. Fundam.* **1970**, *9*, 1−10.

(18) Abdel-Aal, N.; Satoh, K.; Sawada, K. Study of the Adhesion Mechanism of CaCO3 Using a Combined Bulk Chemistry/QCM Technique. *J. Cryst. Growth* **2002**, *245*, 87−100.

(19) Macadam, J.; Parsons, S. A. Calcium Carbonate Scale Formation and Control. *Rev. Environ. Sci. Biotechnol.* **2004**, *3*, 159−169.

(20) Matin, A.; Rahman, F.; Shafi, H. Z.; Zubair, S. M. Scaling of Reverse Osmosis Membranes Used in Water Desalination: Phenomena, Impact, and Control; Future Directions. *Desalination* **2019**, *455*, 135−157.

(21) Liu, Q.; Xu, G.-R.; Das, R. Inorganic Scaling in Reverse Osmosis (RO) Desalination: Mechanisms, Monitoring, and Inhibition Strategies. *Desalination* **2019**, *468*, 114065.

(22) Su, C.; Horseman, T.; Cao, H.; Christie, K.; Li, Y.; Lin, S. Robust Superhydrophobic Membrane for Membrane Distillation with Excellent Scaling Resistance. *Environ. Sci. Technol.* **2019**, *53*, 11801−11809.

(23) Liu, L.; Xiao, Z.; Liu, Y.; Li, X.; Yin, H.; Volkov, A.; He, T. Understanding the Fouling/Scaling Resistance of Superhydrophobic/Omniphobic Membranes in Membrane Distillation. *Desalination* **2021**, *499*, 114864.

(24) Deshmukh, A.; Boo, C.; Karanikola, V.; Lin, S.; Straub, A. P.; Tong, T.; Warsinger, D. M.; Elimelech, M. Membrane Distillation at the Water-Energy Nexus: Limits, Opportunities, and Challenges. *Energy Environ. Sci.* **2018**, *11*, 1177−1196.

(25) Xiao, Z.; Zheng, R.; Liu, Y.; He, H.; Yuan, X.; Ji, Y.; Li, D.; Yin, H.; Zhang, Y.; Li, X.-M.; He, T. Slippery for Scaling Resistance in Membrane Distillation: A Novel Porous Micropillared Superhydrophobic Surface. *Water Res.* **2019**, *155*, 152−161.

(26) Yang, C.; Li, X.-M.; Gilron, J.; Kong, D.-f.; Yin, Y.; Oren, Y.; Linder, C.; He, T. CF4plasma-Modified Superhydrophobic PVDF Membranes for Direct Contact Membrane Distillation. *J. Membr. Sci.* **2014**, *456*, 155−161.

(27) Xu, Y.; Yang, Y.; Sun, M.; Fan, X.; Song, C.; Tao, P.; Shao, M. High-performance desalination of high-salinity reverse osmosis brine by direct contact membrane distillation using superhydrophobic membranes. *J. Appl. Polym. Sci.* **2021**, *138*, 49768.

(28) Zhu, Z.; Zhong, L.; Horseman, T.; Liu, Z.; Zeng, G.; Li, Z.; Lin, S.; Wang, W. Superhydrophobic-Omniphobic Membrane with Anti-Deformable Pores for Membrane Distillation with Excellent Wetting Resistance. *J. Membr. Sci.* **2021**, *620*, 118768.

(29) Lv, Y.; Liu, M. Corrosion and fouling behaviours of copper-based superhydrophobic coating. *Surf. Eng.* **2018**, *35*, 542.

(30) Lv, Y.; Liu, M. Y.; Hui, L. F.; Pavlenko, A. N.; Surtaev, A. S.; Serdyukov, V. S. Heat Transfer and Fouling Rate at Boiling on Superhydrophobic Surface with TiO2 Nanotube-Array Structure. *J. Eng. Thermophys.* **2019**, *28*, 163−176.

(31) Mousavi, S. M. A.; Pitchumani, R. Temperature-Dependent Dynamic Fouling on Superhydrophobic and Slippery Nonwetting Copper Surfaces. *Chem. Eng. J.* **2022**, *431*, 133960.

(32) Ahn, H. S.; Kim, K. M.; Lim, S. T.; Lee, C. H.; Han, S. W.; Choi, H.; Koo, S.; Kim, N.; Jerng, D.-W.; Wongwises, S. Anti-Fouling Performance of Chevron Plate Heat Exchanger by the Surface Modification. *Int. J. Heat Mass Tran.* **2019**, *144*, 118634.

(33) Ferrari, M.; Benedetti, A. Superhydrophobic Surfaces for Applications in Seawater. *Adv. Colloid Interface Sci.* **2015**, *222*, 291−304.

(34) Lv, P.; Xue, Y.; Shi, Y.; Lin, H.; Duan, H. Metastable States and Wetting Transition of Submerged Superhydrophobic Structures. *Phys. Rev. Lett.* **2014**, *112*, 196101.

(35) Bormashenko, E.; Pogreb, R.; Whyman, G.; Erlich, M. Cassie−Wenzel Wetting Transition in Vibrating Drops Deposited on Rough Surfaces: Is the Dynamic Cassie−Wenzel Wetting Transition a 2D or 1D Affair? *Langmuir* **2007**, *23*, 6501−6503.

(36) Bobji, M. S.; Kumar, S. V.; Asthana, A.; Govardhan, R. N. Underwater Sustainability of the "Cassie" State of Wetting. *Langmuir* **2009**, *25*, 12120−12126.

(37) Tsai, P.; Lammertink, R. G. H.; Wessling, M.; Lohse, D. Evaporation-Triggered Wetting Transition for Water Droplets upon Hydrophobic Microstructures. *Phys. Rev. Lett.* **2010**, *104*, 116102.

(38) Nikoo, A. H.; Malayeri, M. R. Incorporation of Surface Energy Properties into General Crystallization Fouling Model for Heat Transfer Surfaces. *Chem. Eng. Sci.* **2020**, *215*, 115461.

(39) Al-Janabi, A.; Malayeri, M. R. A Criterion for the Characterization of Modified Surfaces during Crystallization Fouling Based on Electron Donor Component of Surface Energy. *Chem. Eng. Res. Des.* **2015**, *100*, 212−227.

(40) Al-Janabi, A.; Malayeri, M. R.; Guillén-Burrieza, E.; Blanco, J. Field Evaluation of Coated Plates of a Compact Heat Exchanger to Mitigate Crystallization Deposit Formation in an MD Desalination Plant. *Desalination* **2013**, *324*, 21−33.

(41) Bargir, S.; Dunn, S.; Jefferson, B.; Macadam, J.; Parsons, S. The Use of Contact Angle Measurements to Estimate the Adhesion Propensity of Calcium Carbonate to Solid Substrates in Water. *Appl. Surf. Sci.* **2009**, *255*, 4873−4879.

(42) Doyle, J. D.; Oldring, K.; Churchley, J.; Parsons, S. A. Struvite Formation and the Fouling Propensity of Different Materials. *Water Res.* **2002**, *36*, 3971−3978.

(43) Cai, Y.; Liu, M.; Hui, L. Observations and Mechanism of CaSO4 Fouling on Hydrophobic Surfaces. *Ind. Eng. Chem. Res.* **2014**, *53*, 3509−3527.

(44) Al-Gailani, A.; Sanni, O.; Charpentier, T. V. J.; Barker, R.; Crisp, R.; Bruins, J. H.; Neville, A. Role of Temperature, Roughness and Pressure in Crystallization Fouling from Potable Water on Aluminium Surface. *Therm. Sci. Eng. Prog.* **2021**, *23*, 100911.

(45) Seddon, J. R. T.; Kooij, E. S.; Poelsema, B.; Zandvliet, H. J. W.; Lohse, D. Surface Bubble Nucleation Stability. *Phys. Rev. Lett.* **2011**, *106*, 19−22.

(46) Simonsen, A. C.; Hansen, P. L.; Klösgen, B. Nanobubbles Give Evidence of Incomplete Wetting at a Hydrophobic Interface. *J. Colloid Interface Sci.* **2004**, *273*, 291−299.

(47) Zargarzadeh, L.; Elliott, J. A. W. Thermodynamics of Surface Nanobubbles. *Langmuir* **2016**, *32*, 11309−11320.

(48) Liu, Y.; Zhang, X. A Unified Mechanism for the Stability of Surface Nanobubbles: Contact Line Pinning and Supersaturation. *J. Chem. Phys.* **2014**, *141*, 134702.

(49) Lohse, D.; Zhang, X. Surface Nanobubbles and Nanodroplets. *Rev. Mod. Phys.* **2015**, *87*, 981−1035.

(50) Tyrrell, J. W. G.; Attard, P. Atomic Force Microscope Images of Nanobubbles on a Hydrophobic Surface and Corresponding Force−Separation Data. *Langmuir* **2002**, *18*, 160−167.

(51) Lou, S.-T.; Ouyang, Z.-Q.; Zhang, Y.; Li, X.-J.; Hu, J.; Li, M.-Q.; Yang, F.-J. Nanobubbles on Solid Surface Imaged by Atomic Force Microscopy. *J. Vac. Sci. Technol., B: Microelectron. Nanometer Struct.–Process., Meas., Phenom.* **2000**, *18*, 2573−2575.

(52) Wang, L.; Wang, X.; Wang, L.; Hu, J.; Wang, C. L.; Zhao, B.; Zhang, X.; Tai, R.; He, M.; Chen, L.; Zhang, L. Formation of Surface Nanobubbles on Nanostructured Substrates. *Nanoscale* **2017**, *9*, 1078−1086.

(53) Brenner, M. P.; Lohse, D. Dynamic Equilibrium Mechanism for Surface Nanobubble Stabilization. *Phys. Rev. Lett.* **2008**, *101*, 214505.

(54) Tan, B. H.; An, H.; Ohl, C.-D. Stability of Surface and Bulk Nanobubbles. *Curr. Opin. Colloid Interface Sci.* **2021**, *53*, 101428.

(55) Zhang, X. H. Quartz Crystal Microbalance Study of the Interfacial Nanobubbles. *Phys. Chem. Chem. Phys.* **2008**, *10*, 6842−6848.

(56) Liu, M.; Zhao, W.; Wang, S.; Guo, W.; Tang, Y.; Dong, Y. Study on Nanobubble Generation: Saline Solution/Water Exchange Method. *ChemPhysChem* **2013**, *14*, 2589−2593.

(57) Millare, J. C.; Basilia, B. A. Nanobubbles from Ethanol-Water Mixtures: Generation and Solute Effects via Solvent Replacement Method. *ChemistrySelect* **2018**, *3*, 9268−9275.

(58) Qiu, J.; Zou, Z.; Wang, S.; Wang, X.; Wang, L.; Dong, Y.; Zhao, H.; Zhang, L.; Hu, J. Formation and Stability of Bulk Nanobubbles Generated by Ethanol-Water Exchange. *ChemPhysChem* **2017**, *18*, 1345−1350.

(59) Li, D.; Qi, L.; Liu, Y.; Bhushan, B.; Gu, J.; Dong, J. Study on the Formation and Properties of Trapped Nanobubbles and Surface Nanobubbles by Spontaneous and Temperature Difference Methods. *Langmuir* **2019**, *35*, 12035−12041.

(60) Wang, B.; Wang, M.; Zhang, H.; Sobal, N. S.; Tong, W.; Gao, C.; Wang, Y.; Giersig, M.; Wang, D.; Möhwald, H. Stepwise interfacial self-assembly of nanoparticles via specific DNA pairing. *Phys. Chem. Chem. Phys.* **2007**, *9*, 6313−6318.

(61) Tokunaga, J. Solubilities of Oxygen, Nitrogen, and Carbon Dioxide in Aqueous Alcohol Solutions. *J. Chem. Eng. Data* **1975**, *20*, 41.

(62) Schumpe, A. The Estimation of Gas Solubilities in Salt Solutions. *Chem. Eng. Sci.* **1993**, *48*, 153−158.

(63) Sørensen, H.; Pedersen, K. S.; Christensen, P. L. Modeling of Gas Solubility in Brine. *Org. Geochem.* **2002**, *33*, 635−642.

(64) Maheshwari, S.; Van Der Hoef, M.; Rodríguez Rodríguez, J.; Lohse, D. Leakiness of Pinned Neighboring Surface Nanobubbles Induced by Strong Gas-Surface Interaction. *ACS Nano* **2018**, *12*, 2603−2609.

(65) Petsev, N. D.; Leal, L. G.; Shell, M. S. Universal Gas Adsorption Mechanism for Flat Nanobubble Morphologies. *Phys. Rev. Lett.* **2020**, *125*, 146101.

(66) Sauerbrey, G. n. Verwendung von Schwingquarzen zur Wegung dinner Schichten und zur Mikrowagung. *Physics* **1959**, *155*, 206−222.

(67) Reviakine, I.; Johannsmann, D.; Richter, R. P. Hearing What You Cannot See and Visualizing What You Hear: Interpreting Quartz Crystal Microbalance Data from Solvated Interfaces. *Anal. Chem.* **2011**, *83*, 8838−8848.

(68) Sheikhi, A.; Olsson, A. L. J.; Tufenkji, N.; Kakkar, A.; van de Ven, T. G. M. Overcoming Interfacial Scaling Using Engineered Nanocelluloses: A QCM-D Study. *ACS Appl. Mater. Interfaces* **2018**, *10*, 34553.

(69) Liu, G.; Craig, V. S. J. Improved Cleaning of Hydrophilic Protein-Coated Surfaces Using the Combination of Nanobubbles and SDS. *ACS Appl. Mater. Interfaces* **2009**, *1*, 481−487.

(70) Liu, G.; Wu, Z.; Craig, V. S. J. Cleaning of Protein-Coated Surfaces Using Nanobubbles: An Investigation Using a Quartz Crystal Microbalance. *J. Phys. Chem. C* **2008**, *112*, 16748−16753.

(71) Mason, W. P. Viscosity and Shear Elasticity Measurements of Liquids by Means of Shear Vibrating Crystals. *J. Colloid Sci.* **1948**, *3*, 147−162.

(72) Borovikov, A. P. Measurement of Viscosity of Media by Means of Shear Vibration of Plane Piezoresonators. *Instrum. Exp. Tech.* **1976**, *19*, 223−224.

(73) Kanazawa, K. K.; Gordon, J. G. Frequency of a Quartz Microbalance in Contact with Liquid. *Anal. Chem.* **1985**, *57*, 1770−1771.

(74) Holmes, M.; Keeley, J.; Hurd, K.; Schmidt, H.; Hawkins, A. Optimized Piranha Etching Process for SU8-Based MEMS and MOEMS Construction. *J. Micromech. Microeng.* **2010**, *20*, 115008.

(75) Mayer, T. M.; de Boer, M. P.; Shinn, N. D.; Clews, P. J.; Michalske, T. A. Chemical Vapor Deposition of Fluoroalkylsilane Monolayer Films for Adhesion Control in Microelectromechanical Systems. *J. Vac. Sci. Technol., B: Microelectron. Nanometer Struct.–Process., Meas., Phenom.* **2000**, *18*, 2433.

(76) Wong, J. X. H.; Yu, H.-Z. Preparation of Transparent Superhydrophobic Glass Slides: Demonstration of Surface Chemistry Characteristics. *J. Chem. Educ.* **2013**, *90*, 1203−1206.

(77) Marmur, A. Wetting on Hydrophobic Rough Surfaces: To Be Heterogeneous or Not to Be? *Langmuir* **2003**, *19*, 8343−8348.

(78) Cassie, A. B. D. Contact Angles. *Discuss. Faraday Soc.* **1948**, *3*, 11.

(79) Datta, S.; Pillai, R.; Borg, M. K.; Sefiane, K. Acoustothermal Nucleation of Surface Nanobubbles. *Nano Lett.* **2021**, *21*, 1267.

(80) Israelachvili, J.; Pashley, R. The Hydrophobic Interaction Is Long Range, Decaying Exponentially with Distance. *Nature* **1982**, *300*, 341−342.

(81) Seddon, J. R. T.; Lohse, D.; Ducker, W. A.; Craig, V. S. J. A Deliberation on Nanobubbles at Surfaces and in Bulk. *ChemPhysChem* **2012**, *13*, 2179−2187.

(82) Quach, N. V.-Y.; Li, A.; Earthman, J. C. Interaction of Calcium Carbonate with Nanobubbles Produced in an Alternating Magnetic Field. *ACS Appl. Mater. Interfaces* **2020**, *12*, 43714−43719.

(83) Farid, M. U.; Kharraz, J. A.; Lee, C.-H.; Fang, J. K.-H.; St-Hilaire, S.; An, A. K. Nanobubble-Assisted Scaling Inhibition in Membrane Distillation for the Treatment of High-Salinity Brine. *Water Res.* **2022**, *209*, 117954.

(84) Zhong, L.; Zhang, X.; Ma, J.; Liu, D.; Liu, D.; Wang, Y.; Cui, F.; Wang, W. Synergy of Feed-Side Aeration and Super Slippery Interface in Membrane Distillation for Enhanced Water Flux and Scaling Mitigation. *Water Res.* **2022**, *215*, 118246.

■ NOTE ADDED AFTER ASAP PUBLICATION

This article originally published with an error in the unit scale bar of Figure 5(D). The corrected figure published June 9, 2022.